JOURNAL OF THE AMERICAN CHEMICAL SOCIETY

pubs.acs.org/JACS

Article

Solvation-Structure Design of Multicomponent Eutectic Electrolytes Enabling Al-Rich Alloy Growth in Aqueous Aluminum-Ion Batteries

Yuzhu Liu,[†] Erhai Hu,[†] Binze Yang,[†] Pengbo Zhang,[†] Jin-Xuan Song, Bei-Er Jia, Hong Han Choo, Huaizhu Wang, Dong Xia, Jinpeng Song, Qiang Zhu, Zhenxiang Xing, Zhong Jin,* and Qingyu Yan*

Cite This: https://doi.org/10.1021/jacs.5c17537

Read Online

ACCESS | Metrics & More | Article Recommendations | Supporting Information

ABSTRACT: Aqueous aluminum-ion batteries (AAIBs) offer intrinsic safety, low cost, and high volumetric capacity, but strong hydration of Al^{3+} imposes large desolvation barriers and promotes parasitic reactions, resulting in sluggish deposition and poor durability. Here, we report a deep eutectic electrolyte (DEE) comprising $Al(ClO_4)_3{\cdot}9H_2O$, acetamide, propylene glycol, and water in a molar ratio of 1:40:20:20. This multicomponent formulation creates a dynamically balanced organic−water environment tailored to the strong polarization of Al^{3+}. The resulting electrolyte forms a diverse and uniformly distributed hydrogen-bond network, giving rise to an adaptive solvation structure. This network supports a dual-layer architecture—with a coordination-dominated inner core and a hydrogen-bond-governed shell—that enhances Al^{3+} electrochemistry. It suppresses free-water activity, mitigates hydrogen evolution reaction, and broadens the electrochemical stability window to 3.64 V. These effects lower interfacial resistance and facilitate Al^{3+} transfer kinetics. Consequently, relative to $Al(ClO_4)_3$ (aq) and other substrates (Al/Sn/Ni), the Al^{3+}-DEE promotes Al-enriched codeposition on Zn, forming Al-rich Al−Zn alloys. Coupled with a poly(1,5-diaminoanthraquinone) (PDAAQ) cathode, the Zn/Al^{3+}-DEE/PDAAQ full cell delivers 135 mAh g^{-1} at 1 A g^{-1} with 94% retention during 1700 cycles, along with a higher voltage plateau and reduced polarization. Our findings underscore the importance of solvation-structure design tailored to multivalent-ion characteristics for achieving high-performance AAIBs.

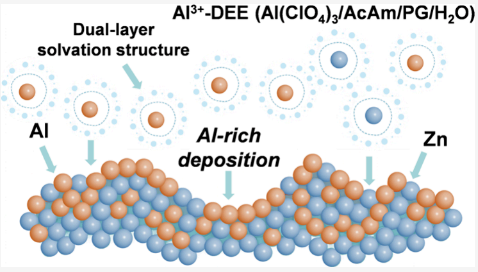

INTRODUCTION

Aqueous aluminum-ion batteries (AAIBs) have recently attracted considerable attention as a promising electrochemical energy storage technology due to their intrinsic safety, low cost, and environmental benignity.[1−4] Aluminum ions possess an ultrahigh theoretical volumetric capacity of 8046 mAh cm^{-3}.[5] Moreover, aluminum is earth-abundant, inexpensive, and environmentally benign, making AAIBs an attractive choice for sustainable energy storage.[6−8] However, Al^{3+} tends to form a highly stable hexahydrated complex, $[Al(H_2O)_6]^{3+}$, in aqueous electrolytes, exhibiting a solvation energy of −4525 kJ mol^{-1}.[9,10] This strong solvation leads to substantial energy barriers for interfacial desolvation, severely limiting the migration and electrodeposition kinetics of Al^{3+} at the electrode interface.[11,12] In particular, the low standard reduction potential of Al^{3+} (−1.667 V vs the standard hydrogen electrode (SHE)) makes selective Al^{3+} deposition thermodynamically unfavorable in aqueous solutions due to competitive hydrogen evolution reaction (HER). In addition, the hydrolysis of Al^{3+} forms passivating $Al(OH)_3$ layers.[13,14] These side reactions jointly hinder ion transport and interfacial kinetics, thereby impairing Coulombic efficiency and cycling stability.

Recent advances in AAIBs have highlighted the importance of rational electrolyte design to simultaneously suppress water reactivity,[15−18] broaden the electrochemical stability window (ESW),[19,20] and improve the kinetics of Al^{3+} deposition.[21−24] Various strategies have been explored, including water-in-salt electrolytes (WISEs),[25−29] organic−inorganic hybrid systems,[30−32] eutectic electrolytes (EEs),[33−36] and electrolyte additives to improve stability.[37−39] However, WISEs suffer from high cost and viscosity, while organic−inorganic hybrid electrolytes often rely on volatile or flammable organic solvents and fail to efficiently regulate the solvation shell of Al^{3+}. EEs, as promising electrolyte candidates, are room-temperature liquids typically formed by hydrogen-bond donors (e.g., alcohols, amides, or carboxylic acids) and hydrogen-bond acceptors (e.g., metal salts). They offer high safety, facile preparation, good chemical stability, and tunable solvation structures, which together contribute to reducing water decomposition and enabling reversible metal plating/stripping. However, most previously reported EEs are hydrated eutectic electrolytes, where the water content far exceeds the organic fraction. Such

Received: October 6, 2025
Revised: December 10, 2025
Accepted: December 12, 2025

ACS Publications

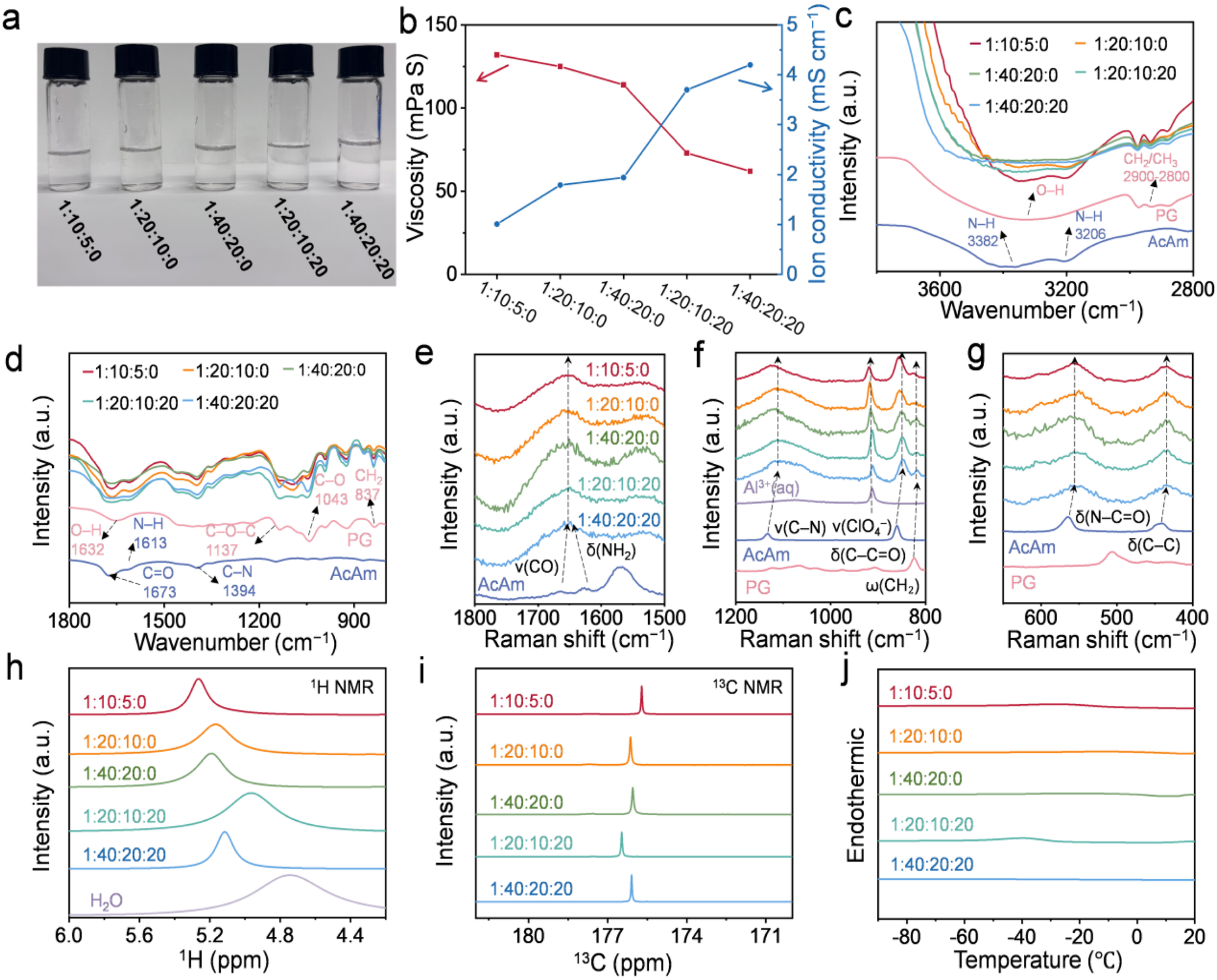

Figure 1. Physicochemical properties and spectroscopic characterization of deep eutectic electrolytes (Al^{3+}-DEEs) with varied compositions. (a) Optical photographs of Al^{3+}-DEEs with different molar ratios of $Al(ClO_4)_3{\cdot}9H_2O$:AcAm:PG:H_2O (1:10:5:0, 1:20:10:0, 1:40:20:0, 1:20:10:20, and 1:40:20:20). (b) Ionic conductivity and viscosity of the Al^{3+}-DEEs at 25 °C. (c, d) FTIR spectra of AcAm, PG, and Al^{3+}-DEEs. (e−g) Raman spectra of 1 M $Al(ClO_4)_3$ aqueous solution, AcAm, PG, and Al^{3+}-DEEs. (h) ^1H NMR and (i) ^{13}C NMR spectra of the Al^{3+}-DEEs. (j) DSC curves of the Al^{3+}-DEEs.

water-dominated systems show a narrow ESW (below 2.6 V) and fail to establish a large, stable organic-dominated hydrogen-bonding network.[34,35]

In this study, we designed a multicomponent deep eutectic electrolyte (DEE). Al^{3+}-DEE comprises $Al(ClO_4)_3{\cdot}9H_2O$, acetamide (AcAm), propylene glycol (PG), and water in a molar ratio of 1:40:20:20. Unlike previously reported Al^{3+}-DEE formulations—whether aimed at suppressing water activity,[40] modulating solvation through strongly coordinating organic components,[41,42] or enhancing conductivity via increased hydration[35]—we focus on constructing a multicomponent, dynamically balanced hydrogen-bond network that effectively modulates the Al^{3+} solvation environment. By combining two organic hydrogen-bond donors (acetamide and propylene glycol) with a tunable water content, we generate a diversified and uniformly distributed hydrogen-bond landscape, rather than a ligand-dominant or water-suppressed structure. This cooperative network accommodates the high charge density and strong polarization of Al^{3+} while preserving nonflammability and intrinsic safety despite the elevated organic fraction. Molecular dynamics simulations reveal that the optimized 1:40:20:20 composition achieves a near-equilibrium hydrogen-bond population among AcAm, PG, and H_2O, producing a more dynamic and adaptive solvation structure than previously reported DEEs. This unique solvation environment gives rise to a dual-layer structure composed of a coordination-dominated inner core and a hydrogen-bond-governed outer shell. AcAm and PG act as competing hydrogen-bond donors, disrupting the rigid water−water network, limiting free-water availability, and weakening Al^{3+}−solvent interactions. As a result, the electrolyte simultaneously suppresses free-water activity, maintains nonflammability and high ionic conductivity, and provides a dynamically balanced solvation environment that facilitates multivalent-ion desolvation. These features collectively enable a stable Al/Zn interphase, fast Al^{3+} electrochemical kinetics, and an expanded ESW of 3.64 V. To overcome the passivating oxide film on Al metal, we screened several nucleation-promoting substrates (Al, Zn, Sn, and Ni) for their ability to facilitate Al deposition.[43−45] Zn proved most effective, enabling Al−Zn codeposition and improving plating/stripping reversibility. Compared to deposits obtained in conventional aqueous electrolytes, those formed in the Al^{3+}-DEE contain significantly higher Al fractions and form Al-rich Al–Zn alloys. Depth-resolved XPS and TOF-SIMS analyses corroborate this enrichment across the deposit depth, showing that the Zn substrate together with the engineered solvation environment promotes the formation of Al-enriched compositions. When paired with a poly(1,5-diaminoanthraquinone) (PDAAQ) cathode,[46] the Zn/Al^{3+}-DEE/PDAAQ full cell delivers a high specific capacity of 135 mAh g^{-1} at the current density of 1 A g^{-1}, with over 94% capacity retention after 1700 cycles, along with a higher discharge voltage plateau, reduced polarization/charge-transfer resistance, and outstanding rate performance. In the Al^{3+}-DEE, Al^{3+} dominates interfacial coordination at the PDAAQ cathode relative to Zn^{2+}. The dual-layer solvation structure—a coordination core with an outer H-bonding shell—effectively suppresses water reactivity, thereby mitigating HER, suppressing Al^{3+} hydrolysis, and limiting Al surface passivation. This unique solvation environment maintains high ionic conductivity, enhances interfacial kinetics for fast Al^{3+} transport, and increases the Al fraction in the codeposited Zn–Al alloy. Overall, this work presents an insightful electrolyte design strategy for advancing high-performance AAIBs.

■ RESULTS AND DISCUSSION

The eutectic frameworks in the designed Al^{3+}-DEEs are established via Lewis acid–base interactions between $Al(ClO_4)_3 \cdot 9H_2O$ and acetamide (AcAm), with propylene glycol (PG) functioning as a hydrogen-bond donor to stabilize the liquid phase and modulate viscosity. The electrolytes were prepared by mixing the components at various molar ratios followed by heating at 80 °C, yielding clear and homogeneous liquids (Figure S1). Increasing the AcAm content led to higher ionic conductivity; however, excessive AcAm disrupted the eutectic balance, resulting in phase solidification upon cooling. Previous studies have shown that polyhydric alcohols such as propylene glycol (PG) can assist metal-ion solvation while simultaneously forming hydrogen bonds with water, thereby stabilizing the eutectic liquid phase and suppressing phase separation.[47,48] Inspired by these findings, we employed PG to enhance liquid-phase stability in our system, though excessive PG content inevitably increased viscosity and compromised conductivity. These results highlight the need to balance the AcAm and PG content to optimize both ionic transport and liquid-phase stability. To reduce compositional complexity and enable systematic comparison, we selected three representative Al^{3+}-DEEs with proportionally increasing AcAm and PG contents but without extra H_2O (1:10:5:0, 1:20:10:0, and 1:40:20:0) for detailed analysis. A balanced organic content helps mitigate ion aggregation and improves ionic conductivity, while an excess of organic components raises viscosity and ultimately hinders ion transport.

In order to address this limitation, small amounts of water were introduced (e.g., 1:20:10:20 and 1:40:20:20), which effectively reduced viscosity and improved ionic conductivity while maintaining liquid-phase stability (Figure 1b). As shown in Figure 1a, all Al^{3+}-DEEs appeared as clear and homogeneous liquids upon preparation. To elucidate the intermolecular interactions in the Al^{3+}-DEEs, we conducted the Fourier transform infrared (FTIR) and Raman spectral analyses on the Al^{3+}-DEE samples. FTIR spectra of Al^{3+}-DEEs (Figure 1c,d) display a broad, smooth absorption band centered around 3200 cm^{-1}, arising from the merged ν(O–H) and ν(N–H) stretching modes of PG and AcAm. Compared with the distinct peaks of pure PG (3382 cm^{-1}) and AcAm (3206 cm^{-1}), this band broadening, together with the redshift of the ν(C═O) stretching and $\delta(NH_2)$ bending modes of AcAm, indicates the formation of C═O···H–O and N–H···O═C hydrogen bonds. The δ(O–H) bending of PG (1632 cm^{-1}) also shows a redshift and pronounced broadening, while characteristic PG bands at 1137 cm^{-1} (ν(C–O–C)), 1043 cm^{-1} (ν(C–O)), and 837 cm^{-1} ($\omega(CH_2)$) shift in both wavenumber and intensity. These changes confirm that both PG and AcAm are integrated into a dynamic hydrogen-bonding network in the Al^{3+}-DEEs.

Raman spectra (Figure 1e–g) provide complementary evidence. The ν(C═O) stretching and $\delta(NH_2)$ bending modes of AcAm merge into a single, blueshifted band in Al^{3+}-DEEs, suggesting reorganization of these vibrations due to coordination with Al^{3+}. The symmetric $\nu(ClO_4^-)$ mode (~914 cm^{-1}) shifts slightly to higher wavenumbers, indicating a transition from free anions to a coordinated state. In addition, characteristic peaks assigned to ν(C–N) (1133 cm^{-1}), δ(C–C═O) (860 cm^{-1}), δ(N–C═O) (566 cm^{-1}), and δ(C–C) (448 cm^{-1}) all exhibit redshifts and broadening.[49−51] These spectral changes reflect strengthened intermolecular hydrogen bonding and increased local polarity, which restrict vibrational freedom and contribute to stabilization of the eutectic framework. ^1H and ^{13}C NMR spectra (Figure 1h,i) further confirm the solvation and hydrogen-bonding environments in Al^{3+}-DEEs. In aqueous $Al(ClO_4)_3$ solution, the H_2O resonance appears at 4.75 ppm but shifts downfield to 5.10–5.30 ppm in Al^{3+}-DEEs, indicating stronger hydrogen bonding or coordination. Meanwhile, the carbonyl carbon of AcAm, resonating at 179 ppm in the pure compound, shifts upfield to 176–177 ppm in Al^{3+}-DEEs, suggesting increased electron shielding due to its incorporation into the hydrogen-bonding network. With increasing AcAm and PG contents (from 1:10:5:0 to 1:40:20:0), the H_2O signal shifts slightly upfield, while the C═O signal moves downfield, implying a gradual transition of the hydrogen-bonding network toward organic species dominance. In the 1:20:10:20 system, the water signal significantly shifted upfield from 5.16 to 4.97 ppm, while the peak of C═O shifts downfield from 176 to 177 ppm. This implies partial disruption of the hydrogen-bonding network, reflected by weaker water integration and attenuated carbonyl interactions. In contrast, the 1:40:20:20 system exhibited negligible changes in the chemical shift of C═O and only a moderate upfield shift of the water signal, suggesting that once the network reaches a steady state in Al^{3+}-DEE, the introduction of water no longer compromises structural stability. Instead, water addition helps reduce viscosity and improves ion transport and conductivity. Collectively, these spectra results confirm that the well-organized hydrogen-bonding network and tailored solvation environment in Al^{3+}-DEEs are key to maintaining liquid-phase stability and promoting efficient ion transport. Differential scanning calorimetry (DSC, Figure 1j) reveals that the eutectic mixture exhibits a significantly depressed melting point below −90 °C. This results from strong hydrogen bonding and coordination, which disrupt individual crystallinity and stabilize the liquid phase. Flammability tests (Figure S2) confirmed that the Al^{3+}-DEEs with ratios of 1:40:20 and 1:40:20:20 are nonflammable, indicating their robustness under practical operating conditions.

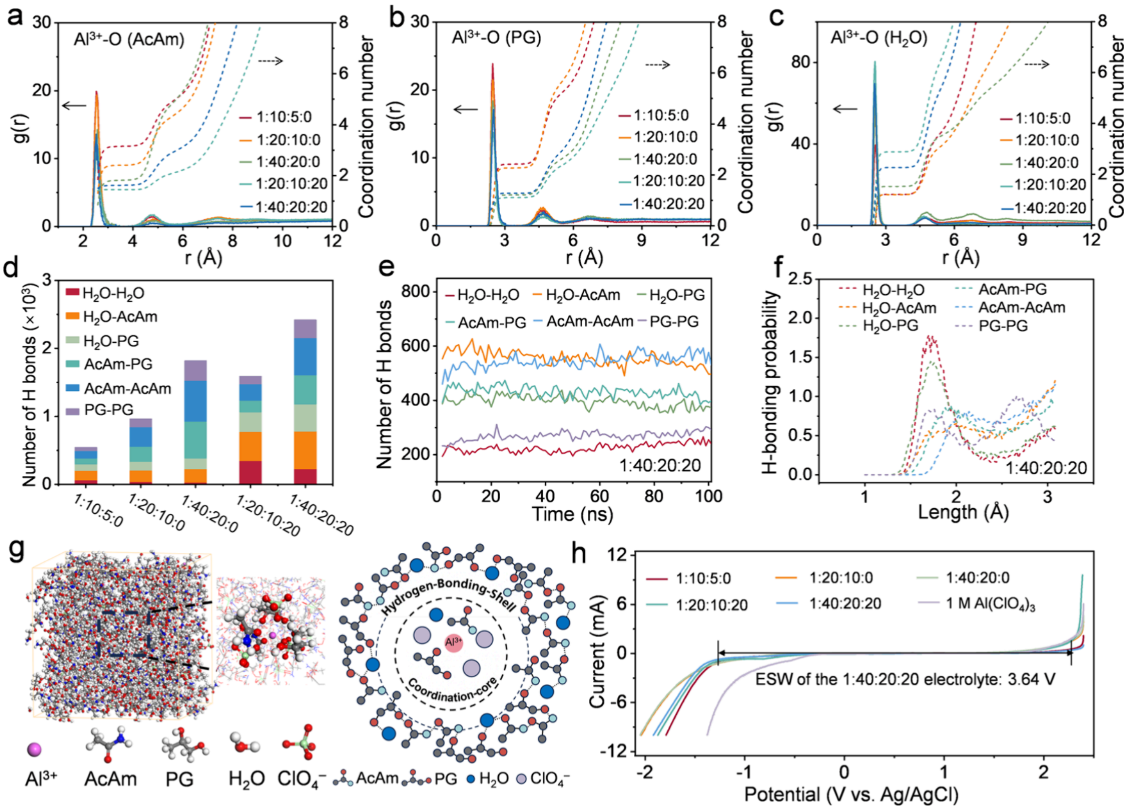

Figure 2. Structural and electrochemical characteristics of Al^{3+}-DEEs with varying compositions. (a−c) Radial distribution functions (RDFs) and coordination numbers for Al^{3+}−O (AcAm), Al^{3+}−O (PG), and Al^{3+}−O (H_2O) obtained by molecular dynamics simulations of the 1:10:5:0, 1:20:10:0, 1:40:20:0, 1:20:10:20, and 1:40:20:20 Al^{3+}-DEEs. (d) Total number of H-bonds in different electrolyte compositions. (e) Time evolution of the number of hydrogen bonds in the 1:40:20:20 Al^{3+}-DEE. (f) Probability distribution of hydrogen-bonding lengths in the 1:40:20:20 Al^{3+}-DEE. (g) Snapshot from MD simulations and schematic illustration of the solvation model of the 1:40:20:20 Al^{3+}-DEE. (h) Electrochemical stability windows (ESWs) of electrolytes with different ratios.

To investigate the Al^{3+} solvation structure of Al^{3+}-DEEs, we performed molecular dynamics (MD) simulations to calculate the coordination numbers between Al^{3+} and various ligands (AcAm, PG, H_2O, and ClO_4^-). As shown in Figure 2a−c and Figure S3, the concentration of AcAm and PG increases, whereas their coordination numbers with Al^{3+} gradually decrease, whereas the coordination numbers of H_2O and ClO_4^- consistently increase. The Al^{3+}−O (H_2O) coordination numbers are 1.21, 1.23, 1.52, 2.88, and 2.26 for 1:10:5:0 to 1:40:20:20 Al^{3+}-DEEs, as summarized in Table S1.

The possible coordination structure (Figure S4) shows that AcAm dominates the first solvation shell in 1:10:5:0 Al^{3+}-DEE, while in 1:40:20:20 Al^{3+}-DEE, H_2O and ClO_4^- become the primary coordinating species. Notably, this trend is supported by NMR spectral shifts, which indicate that AcAm and PG gradually decoordinate from Al^{3+} and increasingly distribute into the surrounding solvation environment. For comparison, we also performed MD simulations for the isocompositional Zn^{2+}-DEE (1:40:20:20 with $Zn(ClO_4)_2$). As shown in Figure S5 and Table S2, Zn^{2+} adopts a weakly associated and AcAm/PG-dominated solvation shell rather than the compact ClO_4^-/H_2O-rich coordination core observed for Al^{3+}. This contrast highlights that the strong, anion-assisted coordination environment is unique to Al^{3+} in DEEs and cannot be replicated by Zn^{2+}.

The H-bonding network in Al^{3+}-DEEs was systematically analyzed by tracking six representative molecular interactions: H_2O−H_2O, H_2O−AcAm, H_2O−PG, AcAm−PG, AcAm−AcAm, and PG−PG (Figure 2d−f and Figures S6 and S7). As Figure 2d shows, in Al^{3+}-DEEs without additional water, the H-bonding network is dominated by AcAm−AcAm and AcAm−PG interactions. Increasing the organic content further densifies this organic-based network. Upon water addition, AcAm−H_2O interactions significantly increase, driving the transition from an "organic-dominated" to an "organic−water-cooperative" H-bonding network. Notably, the distribution of H-bond types becomes more balanced. The multitype network enhances the structural robustness of the H-bonding-shell. As shown in Figure 2e, the three dominant H-bonds in the 1:40:20:20 Al^{3+}-DEE all involve AcAm and remain stable throughout a 100 ns trajectory. In contrast, H_2O−H_2O and PG−PG interactions are much less frequent, suggesting that both water and PG self-association are significantly suppressed in the Al^{3+}-DEE environment. Figure 2f further shows that most H-bonds fall in the range of 1.7−2.2 Å, characteristic of strong H-bonds. Though less probable than H_2O−H_2O interactions, heteromolecular H-bonds are more abundant and widespread, forming the backbone of the Al^{3+}-DEE H-bonding network.

These findings collectively support a dual-layer solvation structure, as illustrated in the MD snapshots and solvation model of the 1:40:20:20 Al^{3+}-DEE (Figure 2g). Because Al^{3+} possesses high charge density and strong polarization, we formulated a balanced organic−water Al^{3+}-DEE to accommodate these characteristics and enhance its electrochemical performance. In this formulation, distinct from Zn^{2+}- and

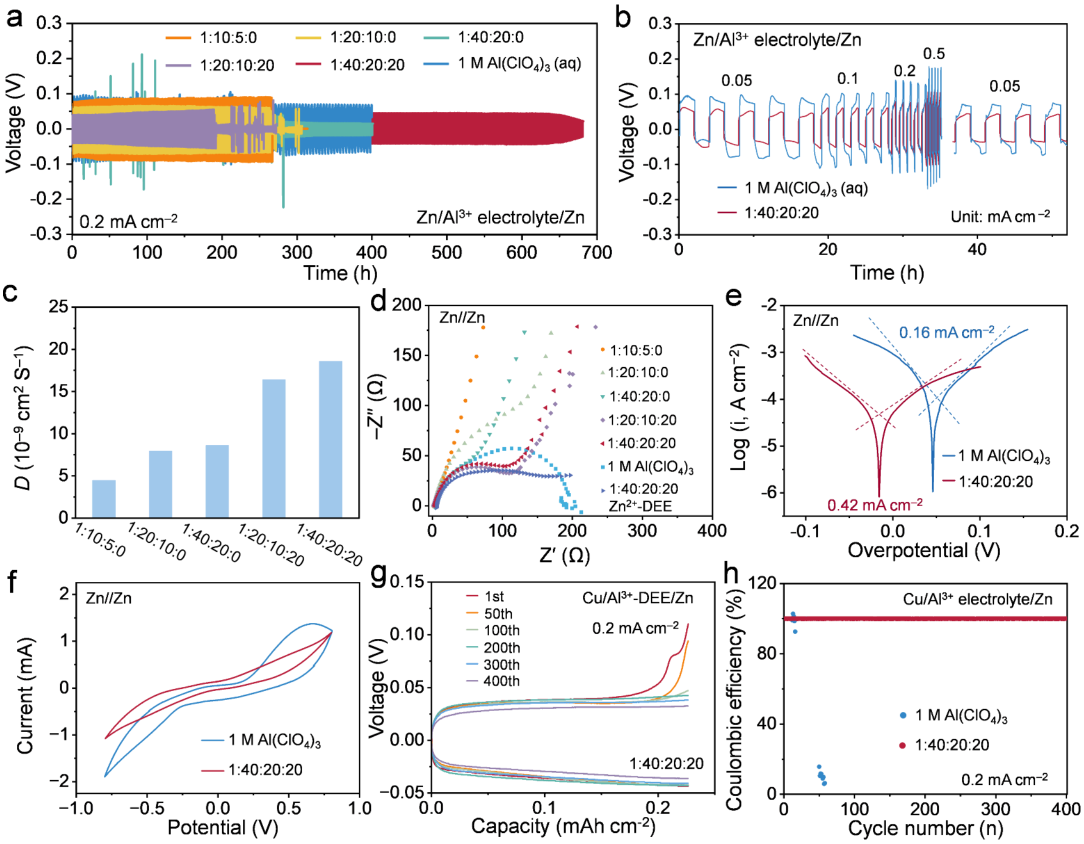

Figure 3. Electrochemical characterization of symmetric and asymmetric cells in different electrolytes. (a) Long-term galvanostatic cycling of Zn//Zn cells in various Al^{3+}-DEE formulations and in a 1 M $Al(ClO_4)_3$ aqueous electrolyte at 0.2 mA cm^{-2}. (b) Rate performance of Zn//Zn cells cycled at different current densities (0.05−0.5 mA cm^{-2}). (c) Apparent Al^{3+} diffusion coefficients (D) of different Al^{3+}-DEE formulations calculated using the Nernst−Einstein equation. (d) Nyquist plots of Zn//Zn symmetric cells in various electrolytes, including Al^{3+}-DEE formulations with different ratios, a 1 M $Al(ClO_4)_3$ aqueous electrolyte, and the isocompositional 1:40:20:20 Zn^{2+}-DEE. (e) Tafel plots and (f) CV profiles of Zn//Zn cells in 1:40:20:20 Al^{3+}-DEE and a 1 M $Al(ClO_4)_3$ aqueous electrolyte. (g) Galvanostatic plating/stripping profiles of Cu//Zn cells in 1:40:20:20 Al^{3+}-DEE at 0.2 mA cm^{-2}. (h) Coulombic efficiency of Cu//Zn cells in 1:40:20:20 Al^{3+}-DEE and in 1 M $Al(ClO_4)_3$ (aq) at 0.2 mA cm^{-2}.

Mg^{2+}-based DEEs with lower organic contents, Al^{3+} preferentially coordinates with small, highly polar ligands (H_2O and ClO_4^-) to form a compact coordination core, while excess organics distribute in the outer shell to build a hydrogen-bonding network. This dual-layer solvation structure suppresses HER and may facilitate Al^{3+} desolvation.

Meanwhile, AcAm and PG are enriched in the outer shell, forming a dense H-bonding-shell that encases the core and restricts anion and water activities. We subsequently evaluated the electrochemical stability windows (ESWs) of different Al^{3+}-DEE formulations via the linear sweep voltammetry method. Compared with 1 M aqueous $Al(ClO_4)_3$, all Al^{3+}-DEEs exhibited significantly broadened ESWs, attributed to the suppression of HER and OER at low and high potentials. The ESWs of different Al^{3+}-DEE formulations are comparable, with the 1:40:20:20 Al^{3+}-DEE exhibiting an ESW of 3.64 V. This enhancement confirms the effectiveness of the dual-layer solvation architecture in suppressing parasitic reactions.

We first examined Al//Al symmetric cells to evaluate aluminum plating/stripping in Al^{3+}-DEEs. Limited cycling was observed at low current densities; however, rapid formation of a passivating oxide on aluminum severely limited the lifetime. We therefore conducted a substrate screening while holding the electrolyte composition fixed at the Al^{3+}-DEE 1:40:20:20—the formulation with the highest ionic conductivity and lowest viscosity—to minimize compositional variables. Symmetric cells with Zn, Ni, and Sn anodes were tested in 1:40:20:20 Al^{3+}-DEE and in a conventional aqueous 1 M $Al(ClO_4)_3$ electrolyte. As shown in Figure S8, the Sn//Sn symmetric cell fails rapidly and short-circuits within 50 h. By contrast, Ni//Ni exhibits a higher polarization voltage, whereas Zn//Zn shows the lowest polarization with smooth and stable profiles. Among these substrates, Zn is identified as the optimal substrate. Galvanostatic cycling was performed at a current density of 0.2 mA cm^{-2} in Zn/Al^{3+}-DEE/Zn symmetric cells to reveal a strong dependence of interfacial polarization on the Al^{3+}-DEE composition (Figure 3a). Formulations with a low organic fraction (e.g., 1:10:5:0 and 1:20:10:0) exhibit large and fluctuating overpotentials together with premature failure, indicating unstable Al plating/stripping. Increasing the organic content and introducing a small amount of water markedly mitigate polarization and extend the lifetime; in particular, the 1:40:20:20 Al^{3+}-DEE sustains long-term cycling with the smallest and most stable voltage hysteresis. This behavior is consistent with the proposed solvation structure, which may facilitate Al^{3+} desolvation, suppress parasitic reactions (e.g., HER), and promote smoother, more reversible deposition/stripping, thereby leading to reduced polarization and prolonged cycling.

https://doi.org/10.1021/jacs.5c17537
J. Am. Chem. Soc. XXXX, XXX, XXX−XXX

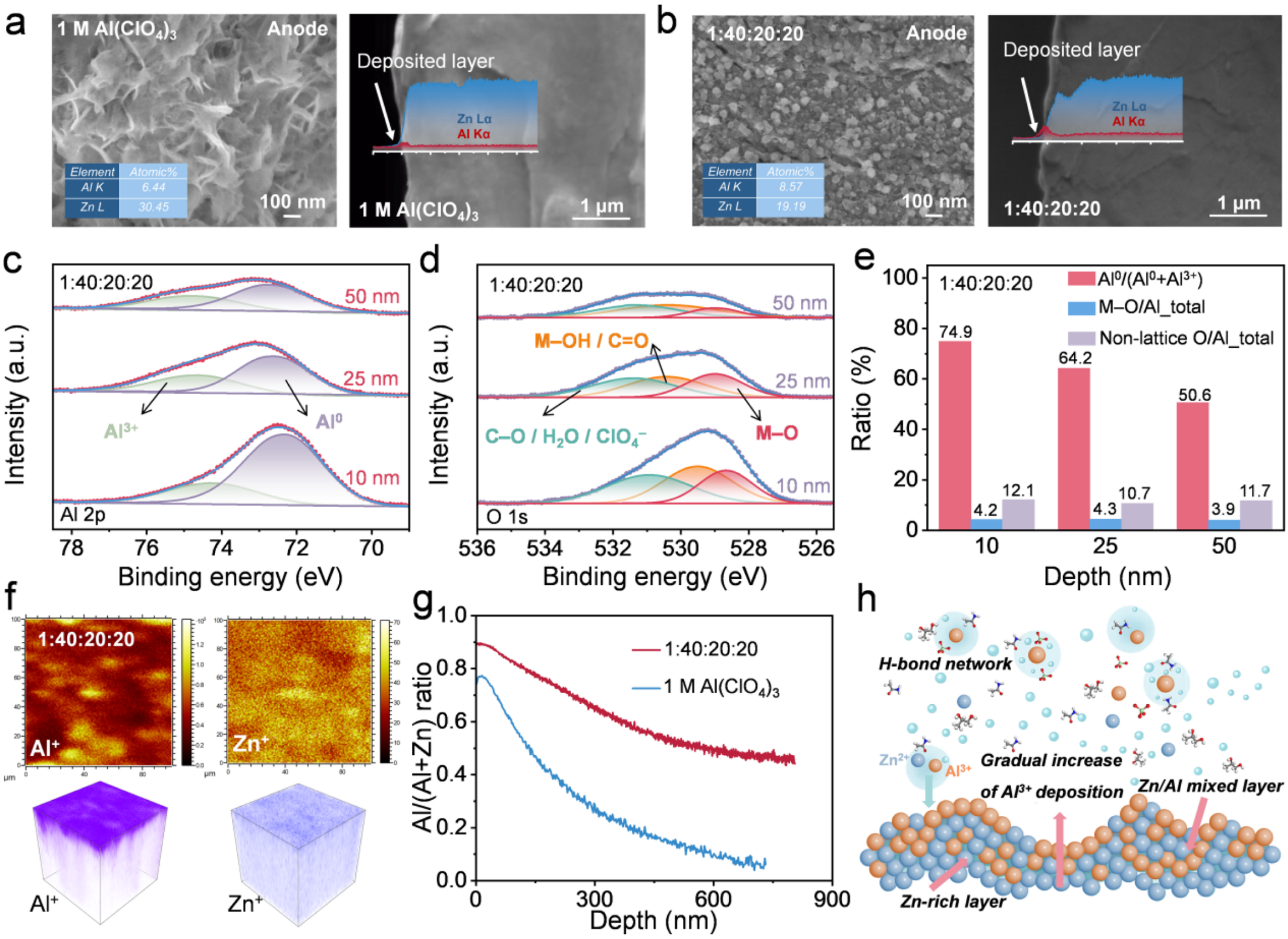

Figure 4. Investigation of Al^{3+} deposition behavior on Zn electrodes in different electrolytes. Surface morphology and cross-sectional SEM−EDS line-scan analysis of Zn anodes cycled in (a) 1 M $Al(ClO_4)_3$ (aq) and (b) 1:40:20:20 Al^{3+}-DEE. Fitted (c) Al 2p spectra and (d) O 1s spectra of the 1:40:20:20 Al^{3+}-DEE sample at etched depths of 10, 25, and 50 nm. (e) Depth-dependent ratios of $Al^0/(Al^0 + Al^{3+})$, M−O/Al_total, and nonlattice O/Al_total in the deposited layer of the 1:40:20:20 Al^{3+}-DEE sample. (f) TOF-SIMS maps and 3D reconstructions of Al^+ and Zn^+ distributions for the 1:40:20:20 Al^{3+}-DEE sample. (g) Depth-dependent Al/(Al + Zn) ratio extracted from TOF-SIMS depth profiling in 1:40:20:20 Al^{3+}-DEE and 1 M $Al(ClO_4)_3$ (aq). (h) Schematic illustration of Al^{3+} deposition on the Zn anode in the Al^{3+}-DEE.

As Figure 3b shows, rate-dependent plating/stripping tests (0.05−0.5 mA cm^{-2}) confirm that the 1:40:20:20 Al^{3+}-DEE sustains low polarization and smooth, stable profiles, with rapid recovery when the current returns to 0.05 mA cm^{-2}. Compared with the 1 M $Al(ClO_4)_3$ aqueous electrolyte, the Al^{3+}-DEE thus delivers markedly improved rate capability and interfacial reversibility. Guided by these symmetric-cell results, the optimal 1:40:20:20 formulation was further investigated to elucidate its interfacial behavior and reaction kinetics. For comparison, Zn//Zn symmetric cells with 1 M $Zn(ClO_4)_2$ (aq) and with an isocompositional Zn^{2+}-DEE (1:40:20:20 with $Zn(ClO_4)_2$) were also evaluated (Figure S9). The cell with aqueous $Zn(ClO_4)_2$ approaches short-circuit within 300 h. The cell with Zn^{2+}-DEE maintains low steady-state overpotentials but exhibits pronounced transient voltage spikes at current reversals (Figure S9d), reflecting a transient overpotential arising from limited interfacial kinetics—sluggish Zn^{2+} desolvation/adsorption and charge transfer. Al^{3+}-DEEs sustain smooth and reversible plating/stripping, whereas Zn^{2+}-DEEs, despite sharing the identical organic framework, fail to establish truly reversible kinetics.

Diffusion coefficients derived from the Nernst−Einstein equation (Figure 3c) further verify that the 1:40:20:20 Al^{3+}-DEE facilitates accelerated ionic transport due to its balanced organic composition. The EIS results are shown in Figure 3d. Al^{3+}-DEE formulations with reduced organic fractions (e.g., 1:10:5:0 and 1:20:10:0) display an extended Warburg tail, indicating predominant diffusion control and pronounced polarization. By contrast, 1:40:20:20 exhibits lower solution resistance (Rs) and charge-transfer resistance (Rct), together with the shortest low-frequency tail, indicating efficient interfacial conduction and weaker diffusion limitation. The aqueous 1 M $Al(ClO_4)_3$ control, instead of showing a diffusion tail, presents a large rs and a broad semicircle corresponding to high rct, reflecting sluggish interfacial charge-transfer processes rather than a diffusion limitation. In comparison, the isocompositional Zn^{2+}-DEE (1:40:20:20 with $Zn(ClO_4)_2$) shows a small semicircle but no well-defined Warburg tail, indicating restricted ion-diffusion behavior and an incomplete interfacial kinetic process, consistent with the transient spikes observed in symmetric-cell cycling. As summarized in Table S3, adjusting the DEE composition leads to clear changes in viscosity, conductivity, diffusion, and interfacial behavior.

https://doi.org/10.1021/jacs.5c17537

Among all tested formulations, the 1:40:20:20 Al^{3+}-DEE achieves balanced transport properties and fast interfacial kinetics and therefore represents the optimal electrolyte system.

The Tafel plots of Zn/Al^{3+} electrolyte/Zn cells (Figure 3e) show that the Al^{3+}-DEE 1:40:20:20 delivers a markedly higher exchange current density (0.42 mA cm^{-2}) than the aqueous 1 M $Al(ClO_4)_3$ electrolyte (0.16 mA cm^{-2}), reflecting faster charge-transfer kinetics. Consistent with the EIS trends, the CV profiles (Figure 3f) show that the 1:40:20:20 Al^{3+}-DEE exhibits more symmetric peaks with a much smaller peak-to-peak separation (ΔEp). By contrast, the $Al(ClO_4)_3$ electrolyte displays an additional oxidation peak near 0.5 V, together with broader peaks, suggesting oxidation/parasitic processes that compete with reversible Al plating/stripping. This difference aligns with the reduced overpotentials and longer lifetimes observed for the 1:40:20:20 Al^{3+}-DEE. Collectively, these results establish that the 1:40:20:20 Al^{3+}-DEE integrates accelerated charge transfer with enhanced reaction kinetics, thereby achieving reduced polarization and superior interfacial kinetics during Al^{3+} plating/stripping.

Asymmetric Cu/Al^{3+} electrolyte/Zn cells were employed to decouple the influence of Zn−Al alloying and to evaluate Al^{3+} plating stability on a chemically distinct substrate. In repeated plating/stripping (Figure 3g,h), the 1:40:20:20 Al^{3+}-DEE maintained stable, low-overpotential profiles with Coulombic efficiency near 100%. By contrast, the aqueous 1 M $Al(ClO_4)_3$ control displayed unstable galvanostatic curves and rapidly decaying Coulombic efficiency (Figure S10a,b). At a current density of 0.2 mA cm^{-2}, the Cu/Al^{3+}-DEE/Zn cells exhibited stable galvanostatic cycling for over 800 h, without significant voltage fluctuation or short-circuiting (Figure S10c). These results underscore the critical role of the H-bond-rich environment in Al^{3+}-DEEs in suppressing parasitic reactions and stabilizing Al^{3+}.

We probed the depth-dependent elemental distribution by XPS depth profiling to corroborate the poor cycling stability of Ni/Al^{3+}-DEE/Ni and Sn/Al^{3+}-DEE/Sn symmetric cells. As shown in Figure S11, the Ni 2p and Sn 3d spectra after plating display only substrate signals, with no detectable Al 2p contribution, confirming that Al deposition is strongly suppressed on these bases. In contrast, Zn provides a favorable substrate for Al deposition. To gain deeper insight into Al deposition on Zn and the role of Al^{3+} electrolytes, Zn electrodes were examined by SEM/EDS after 2 h of galvanostatic plating at 0.2 mA cm^{-2} in each electrolyte. In addition, we conducted XPS and TOF-SIMS depth profiling to track the elemental distribution.

As shown in Figure 4a,b and Figure S12, Zn anodes cycled in 1 M $Al(ClO_4)_3$ exhibit a loose, flake-like, and highly uneven morphology, indicating unstable nucleation and uncontrolled growth. The EDS-derived Al/Zn atomic ratio is only 0.21, suggesting severely limited Al deposition. The corresponding cross-sectional SEM−EDS line scan further shows a markedly weaker interfacial Al signal relative to Zn, consistent with the low Al/Zn ratio. In contrast, the 1:40:20:20 Al^{3+}-DEE electrolyte yields a dense and compact granular morphology with a higher Al/Zn ratio of 0.45, reflecting more uniform and regulated deposition. The cross-sectional line scan shows a stronger Al Kα signal and higher Al/Zn ratio in the DEE electrolyte, with the Al signal extending deeper into the deposited layer than in the aqueous electrolyte. The depth-dependent profiles (insets of Figure 4a,b) clearly reveal the contrasting interfacial compositions formed in the two electrolytes. Taken together, these results clarify that the Al^{3+}-DEE stabilizes the electrode−electrolyte interface by shifting the interphase composition from Zn-rich to more Al-rich codeposition, thereby suppressing dendritic Zn growth and enabling the formation of a denser and more continuous interphase.

Depth profiling XPS results (Figure 4c−e and Figure S13) reveal compositional and chemical-state gradients of Al, O, and Zn within the deposited layer. Peak fitting of Al 2p (Figure 4c) identifies metallic Al^0 (72.6−72.8 eV) and oxidized/hydroxylated Al^{3+} species (74.3−74.5 eV) at all stages of deposition. The overall Al 2p signal intensity increases as the deposit builds, suggesting that Al^{3+}, stabilized by the 1:40:20:20 Al^{3+}-DEE solvation environment, adsorbs onto the Zn surface and undergoes partial reduction to metallic Al, while a fraction of unreduced Al^{3+} remains trapped within the Al−Zn deposited layer. Notably, the $Al^0/(Al^0 + Al^{3+})$ ratio increases during deposition, indicating that progressively more Al^{3+} is reduced to metallic Al (Figure 4e). To characterize the local environment of the Al species, we analyzed the O 1s spectra (Figure 4d). As deposition proceeds, the absolute O 1s intensity rises; however, when normalized to Al_total, the fractions of lattice O (M−O (metal−oxygen), 528.5−529.2 eV) and nonlattice O [M−OH/C=O (530.0−531.0 eV); C−O/H_2O/ClO_4^- (532.5−533.8 eV)] remain essentially constant throughout the deposit (Figure 4e), evidencing a stable oxygen environment for the Al species. This DEE-stabilized interface facilitates sustained Al−Zn codeposition. Meanwhile, the Zn 2p binding energy remains constant at 1021.5 eV, showing no evidence of valence change, while its intensity decreases as the deposit builds (Figure S13). This reflects a compositional gradient in which Zn is enriched near the substrate, whereas Al enrichment develops toward the outer layers. By comparison, the $Al(ClO_4)_3$ (aq) sample shows weak and limited Al signals, with Zn 2p remaining dominant (Figure S14), indicating only a thin Al-containing layer with limited Zn−Al alloying. Taken together, in the 1:40:20:20 Al^{3+}-DEE system, Al^{3+} is partially reduced to metallic Al during deposition while a fraction remains unreduced. Zn and Al codeposit to form a mixed Al−Zn interfacial layer, and as plating continues, Al makes a progressively greater contribution to codeposition. The stable interfacial environment provided by 1:40:20:20 Al^{3+}-DEE, combined with the preferential outward growth of Al from the Zn substrate, enables sustained Al−Zn codeposition with clear Al-preferential growth relative to $Al(ClO_4)_3$ (aq).

To independently verify the trend that Al progressively dominates codeposition, TOF-SIMS maps and 3D reconstructions of the 1:40:20:20 Al^{3+}-DEE sample (Figure 4f,g) reveal an Al^+-rich outer layer with comparatively weaker Zn^+ at the topmost layers, while the $Al(ClO_4)_3$ (aq) sample (Figure S15) exhibits a much less pronounced Al signal. Consistently, the Al/(Al + Zn) depth profiles indicate that DEE maintains a higher Al fraction across the analyzed range, decaying more slowly and remaining elevated (e.g., 0.53 at ~600 nm) relative to $Al(ClO_4)_3$ (aq) (0.12 at the same depth). These observations support a thicker, more continuous Al-rich layer and sustained preferential Al growth in 1:40:20:20 Al^{3+}-DEE, whereas the aqueous electrolyte yields a Zn-enriched interface. The SIMS results therefore corroborate the XPS depth profiles.

We propose a possible deposition model to rationalize these observations (Figure 4h). Specifically, at the early stage of deposition, Zn^{2+} is more readily reduced under the influence of

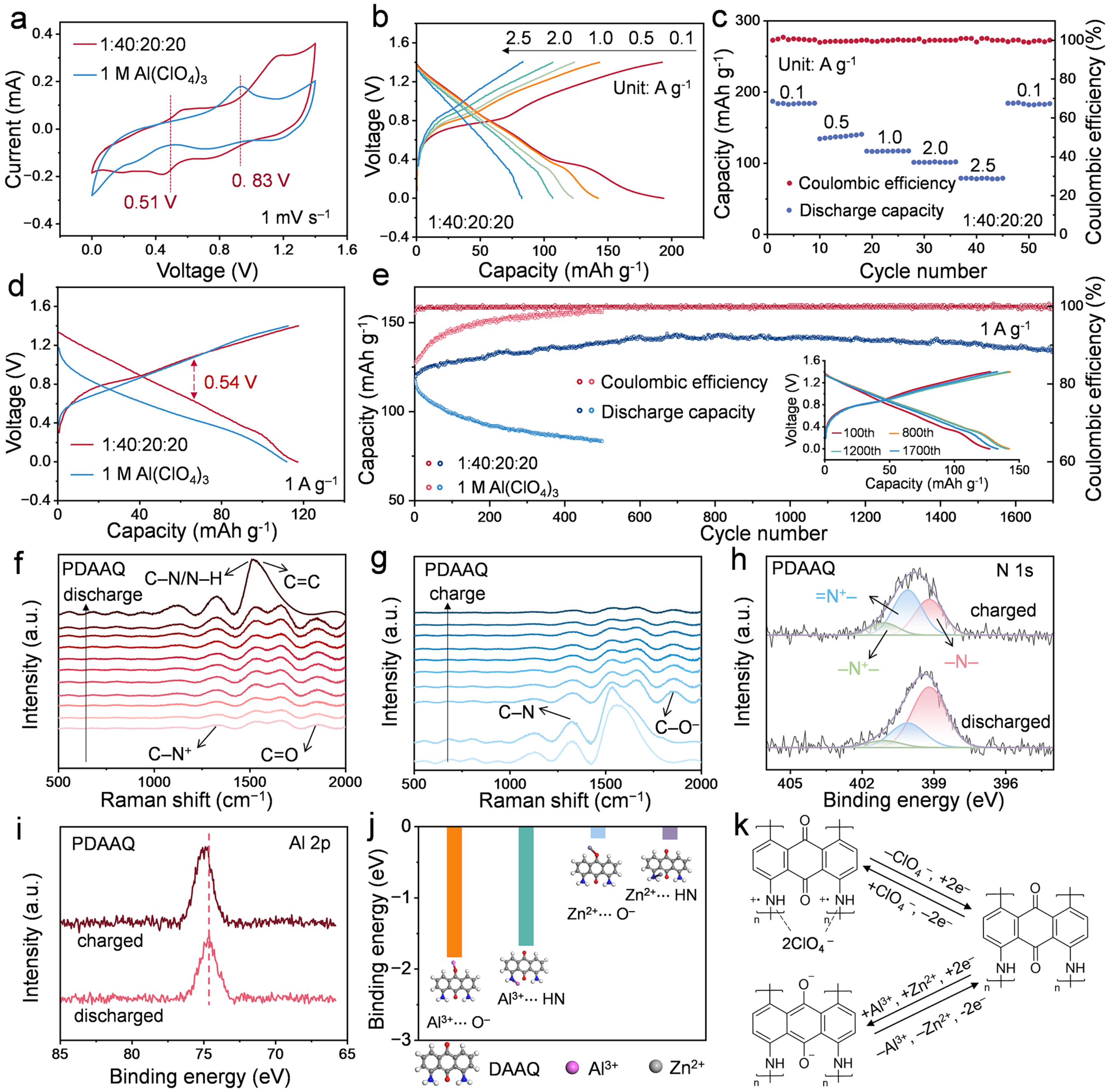

Figure 5. Electrochemical performance and redox mechanism of the Zn/Al^{3+} electrolyte/PDAAQ full cell in 1:40:20:20 Al^{3+}-DEE and 1 M $Al(ClO_4)_3$ electrolytes. (a) CV curves of full cells at a scan rate of 1 mV s^{-1}. (b) Galvanostatic charge–discharge (GCD) profiles of the 1:40:20:20 Al^{3+}-DEE-based full cell at current densities from 0.1 to 2.5 A g^{-1}. (c) Rate performance of the 1:40:20:20 Al^{3+}-DEE-based full cell at various current densities. (d) GCD curves at 1.0 A g^{-1} highlighting the voltage hysteresis. (e) Long-term cycling performance of Zn/Al^{3+} electrolyte/PDAAQ full cells at 1.0 A g^{-1}, comparing 1:40:20:20 Al^{3+}-DEE (dark markers) and $Al(ClO_4)_3$ (aq) (light markers). The inset presents charge–discharge voltage profiles of the Al^{3+}-DEE full cell at different cycles. (f, g) In situ Raman spectra collected during discharge and charge processes, respectively. (h) Fitted N 1s XPS spectra of PDAAQ in charged and discharged states. (i) Al 2p XPS spectra of PDAAQ at charged and discharged states. (j) Binding energies of Al^{3+} and Zn^{2+} interacting with functional groups of the DAAQ monomer. (k) Schematic illustration of the cooperative Al^{3+}/Zn^{2+} coordination and the PDAAQ redox mechanism.

the Zn substrate and preferentially initiates nucleation. Subsequently, Al^{3+} becomes involved in interfacial coreduction, leading to the formation of Al–Zn alloys. Owing to its high charge density and strong polarization capability, Al^{3+} is more prone to adsorb at the nucleation sites. As Al-rich nodules continuously grow at the interface, the strong electrostatic field of Al^{3+} may suppress further Zn^{2+} deposition on these protrusions, thereby mitigating dendrite propagation and promoting a preferential Al growth in the outer layer. Such a deposition process has also been reported in a previous study.[25] In 1:40:20:20 Al^{3+}-DEE, although the first solvation shell of Al^{3+} remains dominated by H_2O/ClO_4^- as in $Al(ClO_4)_3$ (aq), the acetamide–propylene glycol hydrogen-bond network weakens water–water connectivity and lowers water activity. This reduces the energetic barrier for desolvation and outer-sphere reorganization, thereby promoting efficient Al^{3+} charge transfer and interfacial deposition, which explains the enhanced Al fraction and preferential Al growth observed with 1:40:20:20 Al^{3+}-DEE.

We prepared a full cell using poly(1,5-diaminoanthraquinone) (PDAAQ) as the cathode and a zinc foil as the anode to further evaluate the practical applications of the 1:40:20:20 Al^{3+}-DEE system. The synthesis of PDAAQ followed previously reported procedures. To verify the successful synthesis, FTIR analysis was conducted on the monomer 1,5-diaminoanthraquinone (DAAQ) and its polymeric product (PDAAQ) (Figure S16). In DAAQ, a pronounced N−H stretching band appears in the 3300−3400 cm^{-1} region, which significantly diminishes in PDAAQ, indicating that amino groups were converted into secondary amines during polymerization. Meanwhile, new absorptions corresponding to C−N and C═O vibrations emerged in the 1000−2000 cm^{-1} region, confirming the formation of −NH− linkages. The C═O characteristic peak remains present after polymerization but shifts and broadens in PDAAQ, suggesting that the quinone structure is partially retained, with its local electronic environment altered by extended conjugation. These results confirm the successful construction of a conjugated polymer framework via amino condensation.

We then systematically evaluated the electrochemical performance of the Zn/Al^{3+}-DEE/PDAAQ full cell using the 1:40:20:20 Al^{3+}-DEE electrolyte, including its cycling stability, rate capability, and redox mechanism, in comparison with a conventional $Al(ClO_4)_3$ aqueous electrolyte. As shown in Figure 5a, the 1:40:20:20 Al^{3+}-DEE-based full cell exhibits two pairs of well-defined redox peaks centered at ∼0.83/0.51 V, with sharp and symmetric profiles, indicating highly reversible electrochemical reactions. In contrast, the $Al(ClO_4)_3$ (aq) electrolyte shows broader and less distinguishable peaks with larger potential separation, reflecting sluggish kinetics and higher polarization.

CV measurements were performed at different scan rates (0.2−2.0 mV s^{-1}) in both electrolytes to further probe the reaction kinetics (Figure S17). In the 1:40:20:20 Al^{3+}-DEE system, the peak currents increase nearly linearly with the square root of the scan rate, consistent with a diffusion-controlled process. Moreover, the peak shifts with an increasing scan rate are relatively small, further confirming favorable reaction reversibility. By contrast, the $Al(ClO_4)_3$ (aq) system delivers lower current responses and more pronounced potential shifts at higher scan rates, indicative of sluggish ion transport and inferior electrode kinetics. Quantitative analysis using the Randles−Sevcik equation further confirms this difference: the apparent diffusion coefficient (D) of Al^{3+} in the 1:40:20:20 Al^{3+}-DEE electrolyte reaches 2.33×10^{-10} cm^2 s^{-1}, higher than that in the $Al(ClO_4)_3$ (aq) electrolyte (1.59×10^{-10} cm^2 s^{-1}). This enhancement highlights the ability of the hydrogen-bonding network in 1:40:20:20 Al^{3+}-DEE to facilitate Al^{3+} desolvation and transport, thereby underpinning the superior electrochemical kinetics of the full cell.

As shown in Figure 5b,c, the 1:40:20:20 Al^{3+}-DEE-based cell delivers a capacity of 183 mAh g^{-1} at 0.1 A g^{-1}. It maintains 137, 117, 102, and 79 mAh g^{-1} at 0.5, 1.0, 2.0, and 2.5 A g^{-1}, respectively. Full recovery upon returning to 0.1 A g^{-1} evidences good rate capability and reversibility. The rate performance of the $Al(ClO_4)_3$-based cell at different current densities is shown in Figure S18. The corresponding galvanostatic profiles display indistinct discharge plateaus and significant voltage polarization, which become more pronounced at higher current densities. These results highlight the intrinsic kinetic limitations of the $Al(ClO_4)_3$ (aq), leading to poor rate capability and rapid performance decay compared with the 1:40:20:20 Al^{3+}-DEE system. The 1:40:20:20 Al^{3+}-DEE-based full cell exhibits two distinct discharge plateaus with small voltage hysteresis (0.54 V) compared to the $Al(ClO_4)_3$ (aq)-based system, as illustrated in Figure 5d. These results confirm that the 1:40:20:20 Al^{3+}-DEE electrolyte enhances reaction kinetics, thereby suppressing electrode polarization and enabling superior rate performance. Long-term cycling (Figure 5e) highlights the durability of the 1:40:20:20 Al^{3+}-DEE: the cell reaches a peak capacity of 143 mAh g^{-1} during cycling and still delivers 135 mAh g^{-1} after 1700 cycles (≈94% of the peak), while maintaining nearly 100% Coulombic efficiency. The Al^{3+}-DEE electrolyte constructs a stable and compact interphase during the initial cycles. This well-defined interface allows the electrode−electrolyte system to stabilize from the outset, resulting in a high initial Coulombic efficiency and ensuring long-term cycling stability. The XPS results (Figure S19) of the Zn anode during deposition show M−O/Al_total ≈ 0.04 (attributed to Al_2O_3) and (M−OH/C═O)/Al_total ≈ 0.05, an overlapping contribution from Al−OH, carbonyl groups, and possible electrolyte residues, indicating that irreversible byproducts are minor and unlikely to materially affect CE. By contrast, the 1 M $Al(ClO_4)_3$ (aq) cell, despite a comparable initial capacity, undergoes continuous fading within 500 cycles; its initially low CE gradually increases, likely due to early-stage side reactions forming a passivating layer that reduces further parasitic processes, while interfacial degradation still proceeds and capacity cannot be sustained.

Critically, ion-identity control clarifies the cation requirement of the DEE. In an aqueous $Zn(ClO_4)_2$ electrolyte, the Zn/$Zn(ClO_4)_2$/PDAAQ full cell operates normally, confirming that Zn^{2+} can, in principle, participate in the redox behavior of the cathode. As Figure S20 shows, long-term cycling in 1 M $Zn(ClO_4)_2$ shows a comparable initial capacity but a rapid fade within the first few hundred cycles to near zero, indicative of interfacial breakdown. However, when $Al(ClO_4)_3$ (aq) in the 1:40:20:20 DEE (salt:AcAm:PG:H_2O) was replaced with equimolar $Zn(ClO_4)_2$ to yield an isocompositional Zn^{2+}-DEE, the full cell exhibited abnormally high charging capacities but failed to deliver any meaningful discharge, underscoring the lack of reversibility compared with the 1:40:20:20 Al^{3+}-DEE. MD simulations (Figure S5 and Table S2) show that Zn^{2+} in the isocompositional 1:40:20:20 DEE forms a weakly associated, AcAm/PG-dominated solvation shell, in contrast to the compact ClO_4^-/H_2O-rich coordination core of Al^{3+}. Consistent with this weak solvation, the EIS spectra exhibit a small and poorly defined semicircle without a clear Warburg tail, indicating restricted ion diffusion and sluggish interfacial kinetics. Postmortem SEM (Figure S21) further supports this trend: 1 M $Zn(ClO_4)_2$ (aq) shows severe porous/dendritic deposits, 1 M $Al(ClO_4)_3$ (aq) remains rough, and the isocompositional Zn^{2+}-DEE produces irregular and porous morphologies, whereas the 1:40:20:20 Al^{3+}-DEE yields dense and uniform deposits. Together, these results indicate that Al^{3+} is markedly better suited than Zn^{2+} for sustaining stable solvation and interfacial behavior in the organic-rich DEE environment. The large proportion of organic components both dilutes the effective salt concentration and produces a loose, hydrogen-bond-dominated solvation network. Under such conditions, Zn^{2+}—while competent in conventional eutectics with a lower organic content—fails to sustain reversible PDAAQ redox. In contrast, Al^{3+}, with its high charge density, strong Lewis acidity, and robust coordination affinity toward carbonyl oxygen, is capable of adapting to this solvation environment, thereby ensuring efficient electron transfer and stable cycling.

EIS measurements of the full cells before and after cycling were performed to gain deeper insight into ion transport and interfacial behavior (Figure S22). After cycling, the 1:40:20:20 Al^{3+}-DEE cell displays a reduced midfrequency semicircle and a less steep low-frequency branch, signifying lower charge-transfer resistance and mitigated diffusion impedance. This evolution is consistent with the formation of a thin, ion-permeable interphase that suppresses parasitic deposition and preserves percolated ion/electron pathways. In contrast, the 1 M $Al(ClO_4)_3$ (aq) cell shows an enlarged semicircle and a more vertical low-frequency branch after cycling, indicative of progressive interfacial passivation and aggravated mass transport limitations.

To unravel the charge storage mechanism of PDAAQ, we combined CV, in situ Raman spectroscopy, and XPS analysis , complemented by elemental mapping, to elucidate the coordinated redox behavior of carbonyl and imino groups (Figure 5f−k). PDAAQ contains two classes of redox-active sites: carbonyl (C═O) and secondary amine (−NH−). The CV curves exhibit two distinct pairs of reversible redox peaks, suggesting the participation of both functional groups. In situ Raman spectra provide direct evidence of these transformations. Upon discharging (Figure 5f), the 1330 cm^{-1} C−N band strengthens, indicating dedoping from $C-N^+$ to C−N and increased local polarizability. Meanwhile, the 1500 cm^{-1} band strengthens as cationic $C-N^+$ sites ($C-NH^+-$/$C=N^+-$) are reduced to neutral C−N and bond-length alternation decreases, thereby enhancing the coupled ring C═C and C−N/N−H vibration. The C═O stretching region (1650−1680 cm^{-1}) evolves from a doublet into a single dominant band with enhanced intensity at the end of discharge, consistent with the reduction of C═O to $C-O^-$ and the formation of a more homogeneous chemical environment. These changes are fully reversed upon charging (Figure 5g), further demonstrating the reversible redox of carbonyl and imino groups in the 1:40:20:20 Al^{3+}-DEE. XPS analysis provides complementary evidence. The N 1s spectrum (Figure 5h) shows that the charged state exhibits an increased contribution from positively charged nitrogen species ($-N^+-$ and $=N^+-$), whereas the discharged state is dominated by neutral −NH− groups, confirming the reversible redox of imino groups.

EDS mapping before and after prolonged cycling shows that the Al:Zn atomic ratio remains stable at ≈2:1 on the PDAAQ cathode, indicating that both cations consistently participate in the redox process (Figure S23). XPS analysis further corroborates this observation. As shown in Figure 5i, the Al 2p peak exhibits a slight negative shift upon discharge, consistent with an increased local electron density when Al^{3+} coordinates with reduced carbonyl ($C-O^-$). By contrast, the Zn 2p spectra (Figure S24) show negligible binding energy variation between charged and discharged states, implying that Zn^{2+} also interacts with PDAAQ but exerts a weaker coordination effect compared with Al^{3+}. To evaluate their contributions to charge compensation, ICP-OES was performed on the PDAAQ cathode collected at the fully reduced (discharged) state. The resulting Al:Zn molar ratio of 1.9:1 corresponds to 74% of the total charge compensation being provided by Al^{3+} and 26% by Zn^{2+} after normalization by their respective ionic charges (Table S4). Thus, Al^{3+} serves as the primary charge-balancing cation, while Zn^{2+} plays a secondary supporting role. These experimental trends are further rationalized by DFT calculations (Figure 5j). The results show substantially stronger binding of Al^{3+} relative to Zn^{2+} for both $C-O^-$ and −NH− coordination sites (−1.83 and −1.68 eV vs −0.16 and −0.18 eV), indicating that Al^{3+} possesses a significantly higher coordination affinity. Collectively, these results demonstrate that both Al^{3+} and Zn^{2+} are involved in the coordination chemistry of PDAAQ, with Al^{3+} acting as the dominant coordinating ion and Zn^{2+} serving as a supportive contributor. As summarized in Figure 5k, the redox process of PDAAQ proceeds through the cooperative participation of Al^{3+} and Zn^{2+}, with Al^{3+} playing the dominant coordinating role.

CONCLUSIONS

In summary, we have developed a multicomponent Al^{3+}-DEE that establishes a dual-layer solvation structure tailored for Al^{3+} electrochemistry. The balanced organic−water formulation suppresses water reactivity, facilitates Al^{3+} desolvation, and broadens the ESW. In-depth mechanistic analysis shows that the Al^{3+}-DEE promotes Al-enriched codeposition on a Zn host, which is more suitable for Al growth than passivated Al metal and than Sn/Ni. Integrated with a PDAAQ cathode, the Zn/Al^{3+}-DEE/PDAAQ full cell achieves high capacity, stable cycling, and good rate performance. These results show that a high-organic-content DEE tailored to the Al^{3+} solvation structure is an effective route to suppress side reactions, direct Al-rich alloy growth, and enable high-performance AAIBs.

ASSOCIATED CONTENT

Supporting Information

The Supporting Information is available free of charge at https://pubs.acs.org/doi/10.1021/jacs.5c17537.

Experimental section and additional figures and tables, including flammability tests, molecular dynamics simulation snapshots, SEM images, EDS mapping images, TOF-SIMS depth profiles, XPS tests, symmetric-cell tests, CV curves, EIS curves, cycling performance, and battery performance comparisons (PDF)

AUTHOR INFORMATION

Corresponding Authors

Zhong Jin − *State Key Laboratory of Coordination Chemistry, MOE Key Laboratory of Mesoscopic Chemistry, MOE Key Laboratory of High Performance Polymer Materials and Technology, Jiangsu Key Laboratory of Advanced Organic Materials, Suzhou Key Laboratory of Green Intelligent Manufacturing of New Energy Materials and Devices, Tianchang New Materials and Energy Technologies Research Center, Institute of Green Chemistry and Engineering, School of Chemistry and Chemical Engineering, Nanjing University, Nanjing, Jiangsu 210023, P. R. China;* orcid.org/0000-0001-8860-8579; Email: zhongjin@nju.edu.cn

Qingyu Yan − *Energy Research Institute@NTU, Nanyang Technological University, 637141, Singapore; School of Materials Science and Engineering, Nanyang Technological University, 639798, Singapore;* orcid.org/0000-0003-0317-3225; Email: alexyan@ntu.edu.sg

Authors

Yuzhu Liu − *Energy Research Institute@NTU, Nanyang Technological University, 637141, Singapore*

Erhai Hu − *Energy Research Institute@NTU, Nanyang Technological University, 637141, Singapore;* orcid.org/0000-0003-4545-1828

Binze Yang − *State Key Laboratory of Coordination Chemistry, MOE Key Laboratory of Mesoscopic Chemistry, MOE Key Laboratory of High Performance Polymer Materials and Technology, Jiangsu Key Laboratory of Advanced Organic Materials, Suzhou Key Laboratory of Green Intelligent Manufacturing of New Energy Materials and Devices, Tianchang New Materials and Energy Technologies Research Center, Institute of Green Chemistry and Engineering, School of Chemistry and Chemical Engineering, Nanjing University, Nanjing, Jiangsu 210023, P. R. China*

Pengbo Zhang − *State Key Laboratory of Coordination Chemistry, MOE Key Laboratory of Mesoscopic Chemistry, MOE Key Laboratory of High Performance Polymer Materials and Technology, Jiangsu Key Laboratory of Advanced Organic Materials, Suzhou Key Laboratory of Green Intelligent Manufacturing of New Energy Materials and Devices, Tianchang New Materials and Energy Technologies Research Center, Institute of Green Chemistry and Engineering, School of Chemistry and Chemical Engineering, Nanjing University, Nanjing, Jiangsu 210023, P. R. China*

Jin-Xuan Song − *School of Materials Science and Engineering, Nanyang Technological University, 639798, Singapore*

Bei-Er Jia − *School of Materials Science and Engineering, Nanyang Technological University, 639798, Singapore*

Hong Han Choo − *School of Materials Science and Engineering, Nanyang Technological University, 639798, Singapore*

Huaizhu Wang − *State Key Laboratory of Coordination Chemistry, MOE Key Laboratory of Mesoscopic Chemistry, MOE Key Laboratory of High Performance Polymer Materials and Technology, Jiangsu Key Laboratory of Advanced Organic Materials, Suzhou Key Laboratory of Green Intelligent Manufacturing of New Energy Materials and Devices, Tianchang New Materials and Energy Technologies Research Center, Institute of Green Chemistry and Engineering, School of Chemistry and Chemical Engineering, Nanjing University, Nanjing, Jiangsu 210023, P. R. China*

Dong Xia − *Energy Research Institute@NTU, Nanyang Technological University, 637141, Singapore*

Jinpeng Song − *School of Materials Science and Engineering, Nanyang Technological University, 639798, Singapore*

Qiang Zhu − *Institute of Materials Research and Engineering (IMRE), Agency for Science Technology and Research (A*STAR), 138634, Singapore;* orcid.org/0000-0002-1184-0860

Zhenxiang Xing − *Institute of Materials Research and Engineering (IMRE), Agency for Science Technology and Research (A*STAR), 138634, Singapore*

Complete contact information is available at: https://pubs.acs.org/10.1021/jacs.5c17537

Author Contributions

[†]Y.L., E.H., B.Y., and P.Z. contributed equally.

Notes

The authors declare no competing financial interest.

■ ACKNOWLEDGMENTS

The authors acknowledge funding support from the ASTAR MTC programmatic project under grant no. M23L9b0052, Indonesia-NTU Singapore Institute of Research for Sustainability and Innovation (INSPIRASI) under contract no. 6635/E3/KL.02.02/2023, Singapore NRF Singapore-China flagship program under grant no. 023740-00001, and Ministry of Education (MOE) Academic Research Fund (AcRF) under MOET2EP50223-0003. This work was also supported by the National Natural Science Foundation of China (22479074 and 22475096), Equipment Pre-Research and Ministry of Education Joint Fund (8091B02052407), Fundamental Research Program Key Project of Jiangsu Province (BK20253008), Science and Technology Major Project of Jiangsu Province (BG2024013), Key Core Technology Open Competition Project of Suzhou City (SYG2024122), and Open Research Fund of Suzhou Laboratory (SZLAB-1308-2024-TS005).

■ REFERENCES

(1) Elia, G. A.; Marquardt, K.; Hoeppner, K.; Fantini, S.; Lin, R. Y.; Knipping, E.; Peters, W.; Drillet, J. F.; Passerini, S.; Hahn, R. An Overview and Future Perspectives of Aluminum Batteries. *Adv. Mater.* **2016**, *28* (35), 7564−7579.

(2) Yu, H. M.; Zhang, X. F.; Wang, Y. X.; Li, M. L.; Chen, W.; Hu, Z.; Zhu, M. S.; Huang, Y. Activation and Stabilization Strategies of Aluminum Metal Anode Toward High Performance Aqueous Al Metal Batteries. *Adv. Mater.* **2025**.

(3) Hu, E. H.; Jia, B. E.; Zhu, Q.; Xu, J. W.; Loh, X. J.; Chen, J.; Pan, H. G.; Yan, Q. Y. Engineering High Voltage Aqueous Aluminum-Ion Batteries. *Small* **2025**, *21* (28), 2309252.

(4) Jia, B. E.; Thang, A. Q.; Yan, C. S.; Liu, C. T.; Lv, C. D.; Zhu, Q.; Xu, J. W.; Chen, J.; Pan, H. G.; Yan, Q. Y. Rechargeable Aqueous Aluminum-Ion Battery: Progress and Outlook. *Small* **2022**, *18* (43), 2107773.

(5) Yuan, D.; Zhao, J.; Manalastas, W.; Kumar, S.; Srinivasan, M. Emerging rechargeable aqueous aluminum ion battery: Status, challenges, and outlooks. *Nano Materials Science* **2020**, *2* (3), 248−263.

(6) Yan, C. S.; Lv, C. D.; Jia, B. E.; Zhong, L. X.; Cao, X.; Guo, X. L.; Liu, H. J.; Xu, W. J.; Liu, D. B.; Yang, L.; et al. Reversible Al Metal Anodes Enabled by Amorphization for Aqueous Aluminum Batteries. *J. Am. Chem. Soc.* **2022**, *144* (25), 11444−11455.

(7) Yang, B. B.; Wang, Y. K.; Bian, H. F.; Zhang, Y. L.; Du, Y. Y.; Lu, H. B.; Bin, D. A rocking-chair aqueous aluminum-ion battery based on an organic/inorganic electrode. *Chem. Commun.* **2023**, *59* (53), 8246−8249.

(8) Song, Y.; Jiao, S. Q.; Tu, J. G.; Wang, J. X.; Liu, Y. J.; Jiao, H. D.; Mao, X. H.; Guo, Z. C.; Fray, D. J. A long-life rechargeable Al ion battery based on molten salts. *Journal of Materials Chemistry A* **2017**, *5* (3), 1282−1291.

(9) Bock, C. W.; Markham, G. D.; Katz, A. K.; Glusker, J. P. The arrangement of first- and second-shell water molecules in trivalent aluminum complexes: Results from density functional theory and structural crystallography. *Inorg. Chem.* **2003**, *42* (5), 1538−1548.

(10) Wang, D. Y.; Hu, E. H.; Wu, G.; Choo, H.; Franke, C.; Jia, B. E.; Song, J. X.; Sumboja, A.; Anggraningrum, I. T.; Syahrial, A. Z.; et al. Chelation-Driven Electrolyte Design for Enhanced Interface and Electrochemical Window in Aqueous Aluminum Batteries. *Angew. Chem., Int. Ed.* **2025**.

(11) Dou, Q. Y.; Yao, N.; Pang, W. K.; Park, Y.; Xiong, P. X.; Han, X. T.; Rana, H. H.; Chen, X.; Fu, Z. H.; Thomsen, L.; et al. Unveiling solvation structure and desolvation dynamics of hybrid electrolytes for ultralong cyclability and facile kinetics of Zn-Al alloy anodes. *Energy Environ. Sci.* **2022**, *15* (11), 4572−4583.

(12) Lu, C.; Wang, Z. L.; Gao, J.; Li, J. J.; Wei, L. M. Synergistic Effect of Anodic Hydrophilic and Hydrophobic Interfaces for Long Cycle Life Aqueous Aluminum-Zinc Hybrid Ion Batteries. *Adv. Energy Mater.* **2024**, *14* (16), 2304016.

(13) Xiao, R.; Chen, J.; Fu, K.; Zheng, X. Y.; Wang, T.; Zheng, J.; Li, X. G. Hydrolysis Batteries: Generating Electrical Energy during Hydrogen Absorption. *Angew. Chem., Int. Ed.* **2018**, *57* (8), 2219−2223.

(14) Huang, W. J.; Zhang, K.; Yuan, B.; Yang, L. C.; Zhu, M. Predominant intercalation of H+ enables ultrahigh rate capability of oxygen deficient MoO3 for aqueous Al-ion batteries. *Energy Storage Materials* **2022**, *50*, 152−160.

(15) Li, H. Y.; Li, S. J.; Hou, R. L.; Rao, Y.; Guo, S. H.; Chang, Z.; Zhou, H. S. Recent advances in zinc-ion dehydration strategies for optimized Zn-metal batteries. *Chem. Soc. Rev.* **2024**, *53* (15), 7742−7783.

(16) Li, H. Y.; Ren, Y.; Zhu, Y.; Tian, J. M.; Sun, X. Y.; Sheng, C. C.; He, P.; Guo, S. H.; Zhou, H. S. A Bio-Inspired Trehalose Additive for Reversible Zinc Anodes with Improved Stability and Kinetics. *Angew. Chem., Int. Ed.* **2023**, *62* (41), No. e202310143.

(17) Yuan, L. B.; Hao, J. N.; Kao, C. C.; Wu, C.; Liu, H. K.; Dou, S. X.; Qiao, S. Z. Regulation methods for the Zn/electrolyte interphase and the effectiveness evaluation in aqueous Zn-ion batteries. *Energy Environ. Sci.* **2021**, *14* (11), 5669−5689.

(18) Cao, J.; Sun, Y. X.; Zhang, D. D.; Luo, D.; Zhang, L. L.; Chanajaree, R.; Qin, J. Q.; Yang, X. L.; Lu, J. Interfacial Double-Coordination Effect Guiding Uniform Electrodeposition for Reversible Zinc Metal Anode. *Adv. Energy Mater.* **2024**, *14* (2), 2302770.

(19) Xu, D. M.; Ren, X. T.; Li, H. Y.; Zhou, Y. R.; Chai, S. M.; Chen, Y. N.; Li, H.; Bai, L. S.; Chang, Z.; Pan, A. Q.; Zhou, H. S. Chelating Additive Regulating Zn-Ion Solvation Chemistry for Highly Efficient Aqueous Zinc-Metal Battery. *Angew. Chem., Int. Ed.* **2024**, *63* (21), No. e202402833.

(20) Xiao, J.; Adelstein, N.; Bi, Y. J.; Bian, W. J.; Cabana, J.; Cobb, C. L.; Cui, Y.; Dillon, S. J.; Doeff, M. M.; Islam, S. M.; et al. Assessing cathode-electrolyte interphases in batteries. *Nature Energy* **2024**, *9*, 1463.

(21) Raj, M. R.; Zaghib, K.; Lee, G. Advanced aqueous electrolytes for aluminum-ion batteries: Challenges and opportunities. *Energy Storage Materials* **2025**, *78*, No. 104211.

(22) Leung, O. M.; Schoetz, T.; Prodromakis, T.; Ponce de Leon, C. Review-Progress in Electrolytes for Rechargeable Aluminium Batteries. *J. Electrochem. Soc.* **2021**, *168* (5), No. 056509.

(23) Li, M.; Wang, C. S.; Chen, Z. W.; Xu, K.; Lu, J. New Concepts in Electrolytes. *Chem. Rev.* **2020**, *120* (14), 6783−6819.

(24) Heo, J.; Dong, D. J.; Wang, Z. Y.; Chen, F.; Wang, C. S. Electrolyte design for aqueous Zn batteries. *Joule* **2025**, *9* (4), No. 101844.

(25) Zhou, A. X.; Jiang, L. W.; Yue, J. M.; Tong, Y. X.; Zhang, Q. Q.; Lin, Z. J.; Liu, B. H.; Wu, C.; Suo, L. M.; Hu, Y. S.; et al. Water-in-Salt Electrolyte Promotes High-Capacity FeFe(CN)6 Cathode for Aqueous Al-Ion Battery. *ACS Appl. Mater. Interfaces* **2019**, *11* (44), 41356−41362.

(26) Gao, Y. N.; Li, Y.; Yang, H. Y.; Zheng, L. M.; Bai, Y.; Wu, C. Bi-salt electrolyte for aqueous rechargeable aluminum battery. *Journal of Energy Chemistry* **2022**, *67*, 613−620.

(27) Dong, D. J.; Zhao, C. X.; Zhang, X. Y.; Wang, C. S. From Salt in Water, Water in Salt to Beyond. *Adv. Mater.* **2025**, 2418700.

(28) Borodin, O.; Self, J.; Persson, K. A.; Wang, C. S.; Xu, K. Uncharted Waters: Super-Concentrated Electrolytes. *Joule* **2020**, *4* (1), 69−100.

(29) Li, C.; Kingsbury, R.; Zhou, L. D.; Shyamsunder, A.; Persson, K. A.; Nazar, L. F. Tuning the Solvation Structure in Aqueous Zinc Batteries to Maximize Zn-Ion Intercalation and Optimize Dendrite-Free Zinc Plating. *Acs Energy Letters* **2022**, *7* (1), 533−540.

(30) Zhao, Z.; Zhang, Z.; Wang, W.; Xu, T.; Yu, X. Strengthen Water O-H Bond in Electrolytes for Enhanced Reversibility and Safety in Aqueous Aluminum Ion Batteries. *Angew. Chem., Int. Ed.* **2025**, *64* (3), No. e202415436.

(31) Yang, Z. H.; Meng, P. Y.; Jiang, M.; Zhang, X. L.; Zhao, T. S.; Yao, Z. G.; Zhang, J.; Zhang, W.; Fu, C. P. Realizing rechargeable cathode-free aluminum-ion batteries via regulating solvation structure in aqueous-aprotic electrolytes. *Journal of Energy Chemistry* **2024**, *99*, 466−474.

(32) Zhao, Z. C.; Zhang, Z. H.; Xu, T.; Wang, W. B.; Wang, B. F.; Yu, X. B. Solvation Structure Regulation for Highly Reversible Aqueous Al Metal Batteries. *J. Am. Chem. Soc.* **2024**, *146* (3), 2257−2266.

(33) Lu, C.; Wang, Z. L.; Zhang, Y.; Tang, G.; Wang, Y.; Guo, X.; Li, J. J.; Wei, L. M. Aqueous aluminum-zinc hybrid ion batteries with urea-based hydrated eutectic electrolytes. *Nano Energy* **2024**, *120*, No. 109158.

(34) Zhang, X. Y.; Wang, R.; Liu, Z. X.; Ma, Q. W.; Li, H. B.; Liu, Y. Y.; Hao, J. N.; Zhang, S. L.; Mao, J. F.; Zhang, C. F. Regulated Hydrated Eutectic Electrolyte Enhancing Interfacial Chemical Stability for Highly Reversible Aqueous Aluminum-Ion Battery with a Wide Temperature Range of-20 to 60 °C. *Adv. Energy Mater.* **2024**, *14* (22), 2400314.

(35) Luo, X. S.; Wang, R.; Zhang, L. H.; Liu, Z. X.; Li, H. B.; Mao, J. F.; Zhang, S. L.; Hao, J. N.; Zhou, T. F.; Zhang, C. F. Air-Stable and Low-Cost High-Voltage Hydrated Eutectic Electrolyte for High-Performance Aqueous Aluminum-Ion Rechargeable Battery with Wide-Temperature Range. *ACS Nano* **2024**, *18* (20), 12981−12993.

(36) Xu, Y. Z.; Li, Y. X.; Zhang, Q.; Wang, J. M.; Zhao, Q.; Wang, H. Y.; Tang, Y. G.; Chen, J. Weakly Solvating Hydrated Eutectic Electrolyte for High-Performance Aluminum-Ion Batteries with Wide Temperature Range. *J. Am. Chem. Soc.* **2025**, *147*, 35367.

(37) Hao, J. N.; Yuan, L. B.; Zhu, Y. L.; Jaroniec, M.; Qiao, S. Z. Triple-Function Electrolyte Regulation toward Advanced Aqueous Zn-Ion Batteries. *Adv. Mater.* **2022**, *34* (44), 2206963.

(38) Wang, S. X.; Wang, S. N.; Wei, Z. Q.; Wang, Y. Q.; Zhang, D. C.; Chen, Z.; Zhi, C. Y. A parts-per-million scale electrolyte additive for durable aqueous zinc batteries. *Nature Communications* **2025**, *16* (1), 1800.

(39) Wang, Y.; Wang, T. R.; Dong, D. J.; Xie, J.; Guan, Y. P.; Huang, Y. Q.; Fan, J.; Lu, Y. C. Enabling high-energy-density aqueous batteries with bond-anchored electrolytes. *Matter* **2022**, *5* (1), 162−179.

(40) Meng, P. Y.; Huang, J.; Yang, Z. H.; Jiang, M.; Wang, Y. B.; Zhang, W.; Zhang, J.; Sun, B. D.; Fu, C. P. Air-Stable Binary Hydrated Eutectic Electrolytes with Unique Solvation Structure for Rechargeable Aluminum-Ion Batteries. *Nano-Micro Letters* **2023**, *15* (1), 188.

(41) Meng, P. Y.; Yang, Z. H.; Jiang, M.; Zhao, T. S.; Zhang, J.; Fu, C. P. Engineering ternary hydrated eutectic electrolytes to realize rechargeable cathode-free aluminum-ion batteries. *Energy Storage Materials* **2024**, *71*, No. 103663.

(42) Meng, P. Y.; Huang, J.; Yang, Z. H.; Wang, F.; Lv, T.; Zhang, J.; Fu, C. P.; Xiao, W. A Low-Cost and Air-Stable Rechargeable Aluminum-Ion Battery. *Adv. Mater.* **2022**, *34* (8), 2106511.

(43) Jia, B. E.; Hu, E. R.; Hu, Z. Y.; Liew, J. J.; Hong, Z. J.; Guo, Y. Q.; Srinivasan, M.; Zhu, Q.; Xu, J. W.; Chen, J.; et al. Laminated tin-aluminum anodes to build practical aqueous aluminum batteries. *Energy Storage Materials* **2024**, *65*, No. 103141.

(44) Yan, C. S.; Lv, C.; Wang, L. G.; Cui, W.; Zhang, L. Y.; Dinh, K. N.; Tan, H. T.; Wu, C.; Wu, T. P.; Ren, Y.; et al. Architecting a Stable High-Energy Aqueous Al-Ion Battery. *J. Am. Chem. Soc.* **2020**, *142* (36), 15295−15304.

(45) Ran, Q.; Shi, H.; Meng, H.; Zeng, S. P.; Wan, W. B.; Zhang, W.; Wen, Z.; Lang, X. Y.; Jiang, Q. Aluminum-copper alloy anode materials for high-energy aqueous aluminum batteries. *Nature Communications* **2022**, *13* (1), 576.

(46) Ding, Y. Y.; Ren, X.; Chen, D.; Wen, F. J.; Li, T.; Xu, F. Poly(1,5-diaminoanthraquinone) as a High-Capacity Bipolar Cathode for Rechargeable Magnesium Batteries. *Acs Applied Energy Materials* **2022**, *5* (3), 3004−3012.

(47) Deng, W. J.; Deng, Z. P.; Chen, Y. M.; Feng, R. F.; Wang, X. L. Competitive Coordination Structure Regulation in Deep Eutectic

Electrolyte for Stable Zinc Batteries. *Angew. Chem., Int. Ed.* **2024**, *63* (8), No. e202316499.

(48) Hao, J. N.; Yuan, L. B.; Zhu, Y. L.; Bai, X. W.; Ye, C.; Jiao, Y.; Qiao, S. Z. Low-cost and Non-flammable Eutectic Electrolytes for Advanced Zn-I2 Batteries. *Angew. Chem., Int. Ed.* **2023**, *62* (39), No. e202316499.

(49) Li, W. R.; Kong, W. Q.; Liu, W.; Xu, S. F.; Zhu, H. Y.; Liu, S.; Yu, W. H.; Wen, Z. S. Ternary eutectic electrolytes attune the electrode/electrolyte interphase layer toward long-life zinc ion batteries. *Energy Storage Materials* **2024**, *65*, No. 103103.

(50) Song, X. M.; Ge, Y.; Xu, H.; Bao, S. S.; Wang, L.; Xue, X. L.; Yu, Q. C.; Xing, Y. Z.; Wu, Z. A.; Xie, K. F.; et al. Ternary Eutectic Electrolyte-Assisted Formation and Dynamic Breathing Effect of the Solid-Electrolyte Interphase for High-Stability Aqueous Magnesium-Ion Full Batteries. *J. Am. Chem. Soc.* **2024**, *146* (10), 7018−7028.

(51) Dai, T. F.; Yang, B. Z.; Wei, J.; Song, X. M.; Zhang, P. B.; Liu, Y. Z.; Wen, S.; Li, H.; Yu, T. C.; Tie, Z. X.; et al. Environmentally Benign and Long Cycling Mn-Ion Full Batteries Enabled by Hydrated Eutectic Electrolytes and Polycarbonyl Conjugated Organic Anodes. *J. Am. Chem. Soc.* **2025**, *147* (16), 13721−13731.